

# Vertically Graded FeNi Alloys with Low Damping and a Sizeable Spin-Orbit Torque

Rachel E. Maizer,<sup>1,\*</sup> Shuang Wu,<sup>1</sup> Purnima P. Balakrishnan,<sup>2</sup> Alexander J. Grutter,<sup>2</sup> Christy J. Kinane,<sup>3</sup> Andrew J. Caruana,<sup>3</sup> Prabandha Nakarmi,<sup>4</sup> Bhuwan Nepal,<sup>4</sup> David A. Smith,<sup>1</sup> Youngmin Lim,<sup>1</sup> Julia L. Jones,<sup>1</sup> Wyatt C. Thomas,<sup>1</sup> Jing Zhao,<sup>5</sup> F. Marc Michel,<sup>5</sup> Tim Mewes,<sup>4</sup> and Satoru Emori<sup>1,†</sup>

<sup>1</sup>*Department of Physics, Virginia Tech, Blacksburg, VA, USA*

<sup>2</sup>*NIST Center for Neutron Research, National Institute of Standards and Technology, Gaithersburg, MD, USA*

<sup>3</sup>*ISIS-Neutron and Muon Source, STFC Rutherford Appleton Laboratory, Didcot, United Kingdom*

<sup>4</sup>*Department of Physics and Astronomy, University of Alabama, Tuscaloosa, AL, USA*

<sup>5</sup>*Department of Geosciences, Virginia Tech, Blacksburg, VA, USA*

(Dated: June 7, 2024)

Energy-efficient spintronic devices require a large spin-orbit torque (SOT) and low damping to excite magnetic precession. In conventional devices with heavy-metal/ferromagnet bilayers, reducing the ferromagnet thickness to  $\sim 1$  nm enhances the SOT but dramatically increases damping. Here, we investigate an alternative approach based on a 10 nm thick single-layer ferromagnet to attain both low damping *and* a sizable SOT. Instead of relying on a single interface, we continuously break the bulk inversion symmetry with a vertical compositional gradient of two ferromagnetic elements: Fe with low intrinsic damping and Ni with sizable spin-orbit coupling. We find low effective damping parameters of  $\alpha_{\text{eff}} < 5 \times 10^{-3}$  in the FeNi alloy films, despite the steep compositional gradients. Moreover, we reveal a sizable anti-damping SOT efficiency of  $\theta_{\text{AD}} \approx 0.05$ , even *without* an intentional compositional gradient. Through depth-resolved x-ray diffraction, we identify a lattice strain gradient as crucial symmetry breaking that underpins the SOT. Our findings provide fresh insights into damping and SOTs in single-layer ferromagnets for power-efficient spintronic devices.

## I. INTRODUCTION

Spin-orbit torques (SOT) can control the magnetic states of memories and oscillators driven by electric current [1–3]. A widely-studied class of SOT device, known as “Type-Y” [4], can attain especially low power consumption by fulfilling two criteria in the magnetic media: (1) low damping to reduce loss in precessional magnetization dynamics and (2) a strong anti-damping SOT to enable free magnetic precession.

SOTs require symmetry breaking to enable an uncompensated spin accumulation acting on the magnetization [2, 3, 5]. Conventional SOT devices achieve this by heavy-metal/ferromagnet (HM/FM) bilayers [Fig. 1(a)], where the HM/FM interface provides the requisite symmetry breaking. Passing an electric current through the HM, e.g., with a strong spin-Hall effect [6], causes the conduction electron spins with opposite polarizations to deflect toward opposite surfaces of the HM layer. The HM/FM interface develops a non-equilibrium spin accumulation, which is transferred to the FM, exerting SOTs on the magnetization. In addition to the spin-Hall effect in the HM [Fig. 1(a)], various coexisting mechanisms may yield SOTs in HM/FM bilayers [3, 5, 7]. Moreover, the “HM layer” does not necessarily need to consist of heavy elements, as some *3d* transition metals have also been shown to contribute to SOTs [8–11].

Nevertheless, all of these reported mechanisms require a transfer of angular momentum across the HM/FM

interface. Thus, regardless of the mechanism, the net spin accumulation is greatest at the HM/FM interface and decreases sharply within the FM thickness [7, 12, 13]. Consequently, conventional HM/FM bilayers tend to have a thin FM with a thickness of  $t_{\text{FM}} \sim 1$  nm to maximize the torque on the magnetization.

However, while decreasing  $t_{\text{FM}}$  increases the SOTs, it has the undesirable effect of increasing the effective damping. For example, spin-pumping damping scales as  $t_{\text{FM}}^{-1}$  [14], and two-magnon scattering<sup>1</sup> at the HM/FM interface scales as  $t_{\text{FM}}^{-2}$  [16]. In other words, there exists a fundamental trade-off in conventional HM/FM devices: SOTs are enhanced at the expense of higher damping. Attaining low damping *and* strong SOTs remains an outstanding challenge for developing more power-efficient spintronic devices.

Here, we present an encouraging route toward low damping and a sizable anti-damping SOT in *single-layer* FMs. Unlike HM/FM bilayers that break symmetry at the interface, our present approach continuously breaks inversion symmetry within the *bulk* of the FM alloy along its thickness axis [17]. Specifically, we leverage a steep vertical compositional gradient in the FM, as

---

<sup>1</sup> Two-magnon scattering is the decay of uniformly precessing magnetic moments ( $k = 0$  spin wave mode) into a finite-wavelength ( $k \neq 0$ ) spin-wave mode [15]. Two-magnon scattering by itself does not involve energy dissipation from magnetization dynamics to the lattice, so it is not “damping” in the strictest sense. Yet, here, we consider two-magnon scattering to be part of the “effective damping” as it contributes to the broadening of the resonance linewidth (i.e., deteriorates the quality factor of the magnetic precession) and may adversely impact the efficiency and stability of Type-Y SOT devices.

\* maizer@vt.edu

† semori@vt.edu

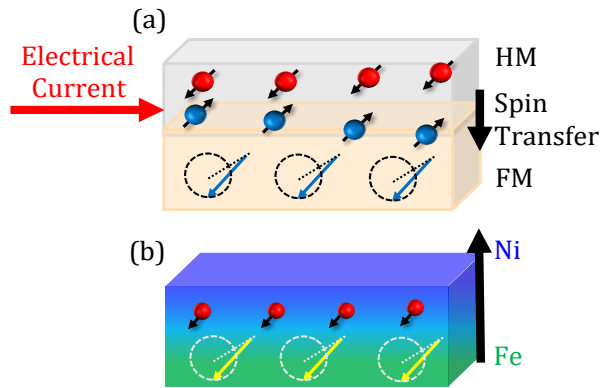


FIG. 1. (a) HM/FM bilayer: the transfer of non-equilibrium spin accumulation across the HM/FM interface generates SOTs, driving precession of the magnetization. (b) Vertically graded alloy: the intentional asymmetry in Fe:Ni composition permits a net non-equilibrium spin accumulation within the bulk, generating SOTs.

illustrated in Fig. 1(b), allowing for the production of spin accumulation within the bulk of the FM. These asymmetric single-layer SOT devices are attractive because they may produce sizable SOTs in thicker FMs, e.g.,  $t_{\text{FM}} \sim 10$  nm [18–20]. Such thick single-layer FMs may maintain low damping while attaining strong SOTs for power-efficient Type-Y SOT devices.

Previous studies [18–20] show SOTs that switch perpendicular magnetization in prototype “Type-Z” devices [4] in  $\sim 10$  nm thick single-layer  $L1_0$  FePt with vertical compositional gradients. More broadly, SOTs have been reported in single-layer FM-HM alloys in which a  $3d$  transition-metal ferromagnet (e.g., Fe or Co) is mixed with a heavy element (e.g., Pt or a rare-earth metal) [18–26]. Yet, these single-layer FM-HM systems possess high damping – e.g., effective damping parameter of  $\alpha_{\text{eff}} \approx 3 \times 10^{-2}$  for FePt [27, 28], which is an order of magnitude greater than  $\alpha_{\text{eff}}$  for many other FMs [29]. Thus, the previous approach to single-layer FMs is unsuitable for Type-Y SOT devices that require low damping.

To pursue low damping, we examined 10 nm thick single-layer FMs with asymmetric compositional gradients of ferromagnetic Fe and Ni [Fig. 1(b)]. We opted for alloys of Fe and Ni because (1) Fe has the lowest Gilbert damping among elemental FMs [29, 30] and (2) Ni has the strongest spin-orbit coupling among elemental FMs [31, 32]. Considering these attributes, we hypothesized the vertically graded FeNi alloys to be viable single-layer FMs that exhibit low damping and strong SOTs for power-efficient devices.

Our article is organized as follows. The nominal structures and the growth conditions of the FeNi films are described in Section II. We present our findings on damping in Section III and current-induced torques

(with particular emphasis on the anti-damping SOT) in Section IV. The observed effective damping remains remarkably low – e.g.,  $\alpha_{\text{eff}} \approx 4.5 \times 10^{-3}$  even with steep vertical Fe-Ni compositional gradients of  $\sim 10$  at.%/nm. Moreover, the anti-damping SOT efficiencies in the FeNi alloys are comparable to those in HM/FM bilayers. Surprisingly, the SOT efficiency does not correlate with the nominal compositional gradient – indicating a nontrivial origin for the observed SOT. In Section V, we show depth-profile characterization of composition and lattice strain to gain further insights into the possible underlying mechanism of the SOT. In Section VI, we discuss the likely contribution of a strain gradient to the sizable SOT in the compositionally symmetric single-layer FM, rivaling SOTs in the FMs with steep compositional gradients. Our work points to the crucial role of an atomic-scale *structural gradient* in enabling a significant SOT. This revelation provides a fresh perspective for engineering low damping and strong SOTs for highly efficient nanomagnetic memories and oscillators.

## II. FILM GROWTH

We focus on three types of 10 nm thick polycrystalline FM FeNi alloy films with an average Fe:Ni ratio footnoteStrictly speaking, the Fe:Ni ratio of 50:50 here refers to the nominal *volume* ratio. The corresponding *atomic* ratio of Fe:Ni, using the tabulated densities and molar masses of Fe and Ni, would be 48:52. of 50:50, as illustrated in Fig. 2:

- nominally symmetric, homogeneous alloy of  $\text{Fe}_{50}\text{Ni}_{50}$  [Fig. 2(a)];
- compositionally graded alloy with Fe on the bottom, denoted as  $\text{Fe}_{100-x}\text{Ni}_x$  with  $x = 0$  at the bottom and  $x = 100$  at the top of the FM [Fig. 2(b)];
- compositionally graded alloy with Ni on the bottom, denoted as  $\text{Fe}_x\text{Ni}_{100-x}$  with  $x = 0$  at the bottom and  $x = 100$  at the top of the FM [Fig. 2(c)].

Each film was grown by dc magnetron sputtering on a Si substrate with a 50 nm thick thermally grown  $\text{SiO}_2$  overlayer, unless otherwise noted. The base pressure prior to deposition was  $\lesssim 3 \times 10^{-8}$  Torr, and the Ar sputtering gas pressure during deposition was 3 mTorr. The deposition rate of each sputtered material was calibrated by x-ray reflectometry.

Each film was seeded by 3 nm thick Ti, followed by 1 nm thick Cu. The Ti layer promotes good adhesion of the film on the  $\text{SiO}_2$  surface, whereas the Cu layer has been reported to reduce effective damping in  $3d$  FMs [33]. The symmetric  $\text{Fe}_{50}\text{Ni}_{50}$  layer [Fig. 2(a)] was grown by co-sputtering Fe and Ni targets at the same deposition rate. The compositionally graded  $\text{Fe}_{100-x}\text{Ni}_x$  [Fig. 2(b)] and  $\text{Fe}_x\text{Ni}_{100-x}$  [Fig. 2(c)] layers were grown by continuously ramping the sputtering power for the Fe and Ni targets.

In particular, to grow  $\text{Fe}_{100-x}\text{Ni}_x$ , the sputtering power of the Fe (Ni) target was ramped linearly from 97 W to 0 W (from 0 W to 80 W); to grow  $\text{Fe}_x\text{Ni}_{100-x}$ , the sputtering power ramping directions were reversed. As we will show in Sec. V, this deposition protocol resulted in an approximately linear compositional gradient in the bulk of  $\text{Fe}_{100-x}\text{Ni}_x$  and  $\text{Fe}_x\text{Ni}_{100-x}$ . Finally, each film was capped with 1 nm thick Cu and 3 nm thick Ti for protection from oxidation. As illustrated in Fig. 2, the Ti/Cu seed and Cu/Ti capping layers are nominally symmetric. With the stack structures in Fig. 2(b,c), the steep compositional gradient within FeNi is the only intentional source of symmetry breaking.

### III. DAMPING

We first present the impact of the steep compositional gradient on magnetic damping in the FeNi films with ferromagnetic resonance (FMR) spectroscopy. Since our study is restricted to room temperature, we might surmise that damping is dominated by the resistivity-like mechanism [34, 35], where damping increases with more electronic scattering. However, the sheet resistances of the three films, obtained from four-point van der Pauw measurements, vary by only  $\sim 10\%$  – so that the resistivity-like damping might be similar. In fact, it is not immediately clear how the steep compositional gradient should impact damping here. While damping has been widely studied in bilayers, multilayers, and homogeneous alloy films [29, 36–38], there appear to be no published studies of damping in compositionally graded single-layer FM films.

In our present study, we define the “effective” damping parameter  $\alpha_{\text{eff}}$  to be the sum of intrinsic and extrinsic contributions,

$$\alpha_{\text{eff}} = \underbrace{\alpha_{\text{int}}}_{\text{intrinsic}} + \underbrace{\alpha_{\text{TMS}}}_{\text{extrinsic}}. \quad (1)$$

The intrinsic component  $\alpha_{\text{int}}$  in Eq. 1 captures the viscous Gilbert damping, which causes the FMR linewidth to scale linearly with the excitation frequency [36, 39]. The damping contribution from spin pumping across interfaces is neglected because spin-

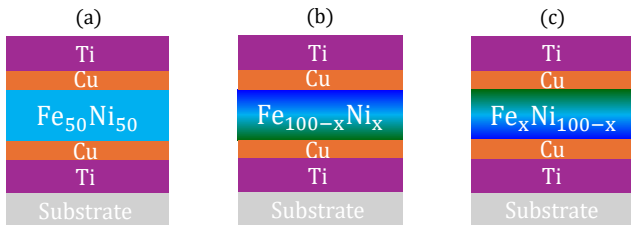


FIG. 2. Nominal film structures for (a) compositionally symmetric  $\text{Fe}_{50}\text{Ni}_{50}$ , (b) compositionally asymmetric  $\text{Fe}_{100-x}\text{Ni}_x$ , and (c) compositionally asymmetric  $\text{Fe}_x\text{Ni}_{100-x}$ .

orbit coupling (hence spin dissipation) is weak in Ti and Cu [31]. Since our FeNi films are significantly thinner than the skin depth for typical FeNi alloys, the eddy-current damping is also considered negligible.

We attribute the extrinsic component  $\alpha_{\text{TMS}}$  in Eq. 1 to non-Gilbert magnetic relaxation – namely, two-magnon scattering (TMS), a decay of the uniform FMR mode into magnon modes due to magnetic inhomogeneity in the film [15, 40]. Two-magnon scattering often manifests in a nonlinear frequency dependence of the FMR linewidth. However, when two-magnon scattering is small relative to the intrinsic damping,  $\alpha_{\text{TMS}}$  may simply appear as a correction to  $\alpha_{\text{int}}$ , derived from the linear slope of the FMR linewidth over a limited frequency range [16, 41].

We can disentangle the intrinsic and extrinsic damping parameters through different FMR measurement configurations [33, 41].

- When the film is magnetized out-of-plane, there exist no magnon states degenerate with the FMR frequency, and two-magnon scattering is suppressed ( $\alpha_{\text{TMS}} = 0$ ) [15, 36, 39]. Hence,  $\alpha_{\text{int}}$  is measured in the out-of-plane FMR configuration [Sec. III A].
- When the film is magnetized in-plane, there are magnon modes degenerate with the FMR mode, allowing for two-magnon scattering to occur [15, 36, 39]. Thus, the in-plane FMR configuration [Sec. III B] measures  $\alpha_{\text{eff}}$  including both the intrinsic and extrinsic contributions [Eq. 1]. In the 10 nm thick FMs here, the source of two-magnon scattering is not necessarily restricted to the film interfaces [16] but may also emerge from inhomogeneity in the FM bulk [15, 41].

We assume that  $\alpha_{\text{int}}$  is identical between the out-of-plane and in-plane configurations. This is likely reasonable because Gilbert damping is expected to be isotropic in Fe and Ni at room temperature [42]. While quantifying  $\alpha_{\text{int}}$  is critical for examining the fundamental origin of damping, we note that  $\alpha_{\text{eff}}$  may be crucial for practical applications, especially Type-Y SOT devices, in which the magnetization lies in-plane [1, 2, 4].

#### A. Intrinsic damping

To conduct out-of-plane FMR measurements, each sample was placed on a W-band shorted waveguide in a superconducting magnet, allowing for a high applied field ( $\geq 4$  T) to saturate the magnetization completely out-of-plane [41, 43]. Figure 3(a) shows the frequency  $f$  dependence of the half-width-at-half-maximum FMR linewidth  $\Delta H^{\text{OP}}$  for the three FeNi films. We quantify  $\alpha_{\text{int}}$  from the linear fit of  $\Delta H^{\text{OP}}$  vs  $f$ ,

$$\mu_0 \Delta H^{\text{OP}} = \mu_0 \Delta H_0^{\text{OP}} + \frac{2\pi}{\gamma} \alpha_{\text{int}} f, \quad (2)$$

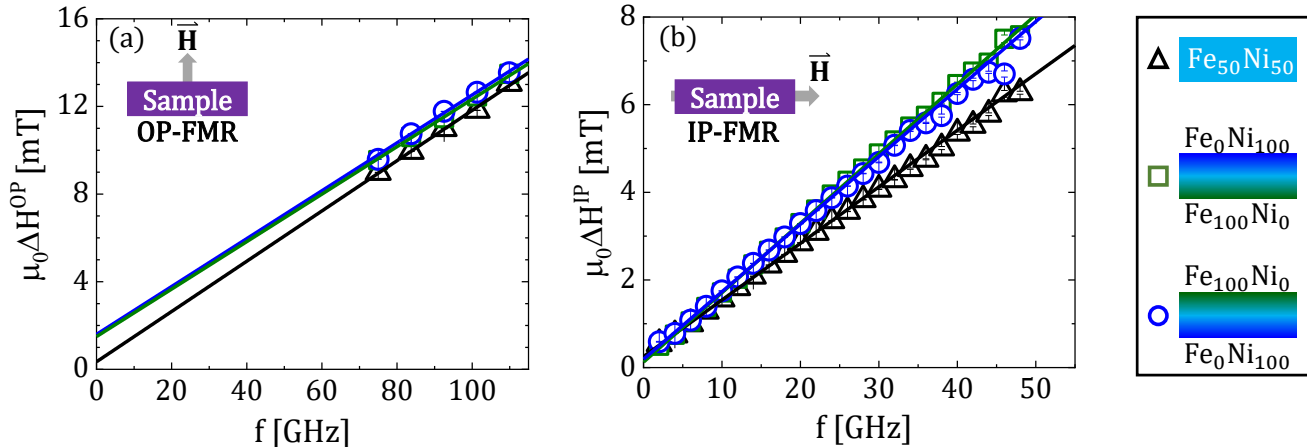


FIG. 3. FMR linewidth vs frequency for  $\text{Fe}_{50}\text{Ni}_{50}$  (black triangle),  $\text{Fe}_{100-x}\text{Ni}_x$  (green square), and  $\text{Fe}_x\text{Ni}_{100-x}$  (blue circle) with FMR configuration (a) out-of-plane and (b) in-plane.

where  $\mu_0$  is the permeability of free space,  $\Delta H_0^{\text{OP}}$  is the zero-frequency linewidth, and  $\gamma/(2\pi) = 29.2$  GHz is the gyromagnetic ratio (derived from the  $f$  dependence of the resonance field, fit with the Kittel equation [41, 43]).

As summarized in Table I, we find that the intrinsic Gilbert damping parameters of the three films,  $\alpha_{\text{int}} \approx (3.2 - 3.3) \times 10^{-3}$ , are identical within the experimental uncertainty of  $\approx 0.1 \times 10^{-3}$ . Remarkably, the steep compositional gradients do not impact intrinsic Gilbert damping in these films.

From this invariance against the compositional gradient, we deduce that the average global composition (here, Fe:Ni ratio of 50:50), rather than the local inhomogeneities, predominantly govern  $\alpha_{\text{int}}$  of the 10 nm thick FeNi films. The finding is also aligned with previous experiments reporting *intrinsic* Gilbert damping to be invariant with compositional profiles [37]. Although a rigorous explanation of the underlying mechanism requires further work, we speculate that the ferromagnetic exchange length [44] may play a critical role. As long as the graded FM thickness is below or comparable to the exchange length (likely up to  $\sim 10$  nm in the alloys here [44, 45]), the impact of local compositional variations on  $\alpha_{\text{int}}$  may be averaged out.

Regardless of the mechanism, we have demonstrated low intrinsic damping – e.g., a full order of magnitude lower than that in FePt [27, 28] used in graded SOT devices [18–20] – even with a steep vertical compositional gradient of  $\sim 10$  at.%/nm. This finding is highly promising for engineering symmetry-broken FMs for Type-Y SOT devices.

While  $\alpha_{\text{int}}$  is unaffected by the compositional gradient, we observe a clear difference in  $\Delta H_0^{\text{OP}}$  (vertical intercept in Fig. 3(a)) between the FeNi films with and without the gradient. In particular,  $\Delta H_0^{\text{OP}}$  is several times greater for the graded  $\text{Fe}_{100-x}\text{Ni}_x$  and  $\text{Fe}_x\text{Ni}_{100-x}$  samples compared to the homogeneous  $\text{Fe}_{50}\text{Ni}_{50}$  sample. This observation

is in line with the notion that  $\Delta H_0^{\text{OP}}$  in the simple linear fit [Eq. 2] is sensitive to local inhomogeneity [36, 39].

## B. Effective damping

We employed an FMR spectrometer based on a coplanar waveguide (details in Ref. [43, 46]). The frequency  $f$  dependence of the in-plane half-width-at-half-maximum FMR linewidth  $\Delta H^{\text{IP}}$  is shown in Fig. 3(b). We quantify the effective damping parameter  $\alpha_{\text{eff}}$  through

$$\mu_0 \Delta H^{\text{IP}} = \mu_0 \Delta H_0^{\text{IP}} + \frac{2\pi}{\gamma} \alpha_{\text{eff}} f. \quad (3)$$

As summarized in Table I, the values of  $\alpha_{\text{eff}}$  for  $\text{Fe}_{100-x}\text{Ni}_x$  and  $\text{Fe}_x\text{Ni}_{100-x}$  with steep vertical compositional gradients are about 20% greater than the homogeneous  $\text{Fe}_{50}\text{Ni}_{50}$  film. The larger  $\alpha_{\text{eff}}$  may be accounted for by enhanced bulk two-magnon scattering induced by local magnetic inhomogeneities in the FM bulk [15, 41], perhaps tied to the intentional compositional gradient within the FM. We note that  $\alpha_{\text{eff}}$  for  $\text{Fe}_{50}\text{Ni}_{50}$  is still greater than  $\alpha_{\text{int}}$  by  $\approx 10\%$ , which suggests that weak two-magnon scattering is also present

TABLE I. Damping parameters quantified from the FMR results in Fig. 3. The error bars are obtained from the square root of the diagonal of the covariance matrix associated with the weighted linear fit slopes [Fig. 3].

	$\text{Fe}_{50}\text{Ni}_{50}$	$\text{Fe}_{100-x}\text{Ni}_x$	$\text{Fe}_x\text{Ni}_{100-x}$
$\alpha_{\text{int}} (10^{-3})$	$3.34 \pm 0.13$	$3.15 \pm 0.09$	$3.18 \pm 0.11$
$\alpha_{\text{eff}} (10^{-3})$	$3.77 \pm 0.02$	$4.63 \pm 0.01$	$4.50 \pm 0.03$

in this nominally homogeneous sample.

Despite the likely presence of two-magnon scattering, the effective damping remains low with  $\alpha_{\text{eff}} < 5 \times 10^{-3}$  for all three samples. Even with a steep, intentional compositional gradient,  $\alpha_{\text{eff}}$  here is an order of magnitude lower than the reported damping parameter of FePt [27, 28]. Furthermore, it is lower than  $\alpha_{\text{int}} \approx (6 - 7) \times 10^{-3}$  for the oft-studied prototypical soft FM of permalloy (Fe<sub>20</sub>Ni<sub>80</sub>) [29, 47]. The demonstrated low effective damping in the FeNi films here constitutes a crucial step toward power-efficient SOT devices.

#### IV. CURRENT-INDUCED TORQUES

We demonstrated in Sec. III that the FeNi films meet the criterion of low damping for Type-Y SOT devices. We now show that a sizable anti-damping SOT – also known as “damping-like” SOT – emerges within the bulk of these FeNi films. Spin-torque FMR (ST-FMR) measurements were performed on 50  $\mu\text{m}$  wide lithographically patterned strips to examine torques induced by current, including the anti-damping SOT and the classical Oersted field torque [48]. An in-plane applied magnetic field at an angle  $\phi$  from the current axis defines the precessional axis. Further details of the ST-FMR method are in Appendix A.

We highlight two key observations from the ST-FMR spectra in Fig. 4. First, Fe<sub>100-x</sub>Ni<sub>x</sub> and Fe<sub>x</sub>Ni<sub>100-x</sub> exhibit opposite signal polarity [Fig. 4(b,c)]. This is unsurprising since the opposite compositional gradients are expected to yield opposite current-induced torques, captured in the polarity of the rectified voltage  $V_{\text{mix}}$ . Second, Fe<sub>50</sub>Ni<sub>50</sub> yields a clear ST-FMR response [Fig. 4(a)], comparable in magnitude to Fe<sub>100-x</sub>Ni<sub>x</sub> and Fe<sub>x</sub>Ni<sub>100-x</sub>. This finding is surprising – because in such a symmetric sample, the current-induced spin accumulations and Oersted field should average to zero. In other words, we would expect that Fe<sub>50</sub>Ni<sub>50</sub> without any intentional symmetry breaking to exhibit little or no current-induced torques.

In this section, we investigate how the current-induced torques depend on the compositional gradients – and address how a sizable torque can emerge in the nominally symmetric Fe<sub>50</sub>Ni<sub>50</sub> sample. We evaluate the anti-damping SOT in Sec. IV A and the Oersted field<sup>2</sup> in Sec. IV B. Then, in Sec. IV C, we gain partial insights into the origin of the anti-damping SOT by comparing it with the Oersted field torque.

<sup>2</sup> There could also be a “field-like” SOT that acts similarly to the Oersted field torque, but we show that it is likely very small.

#### A. Anti-damping SOT

Analyzing the shape of ST-FMR spectra (i.e., the ratio of the symmetric and antisymmetric Lorentzian components) is a common approach to quantify the anti-damping SOT [48, 50]. However, ST-FMR spectra can contain spurious contributions from spin-pumping and thermoelectric voltage signals [50–53]. Moreover, the shape of a ST-FMR spectrum can be affected by a microwave current phase lag [54]. Therefore, we employed a more direct approach: injecting an additional dc current density  $J_{\text{dc}}$  and monitoring its effect on the linewidth  $\Delta H$ . A dc-current-induced anti-damping SOT manifests in a linear shift in  $\Delta H$  with  $J_{\text{dc}}$  [48, 55, 56].

Such a linear change is indeed observed for all three FeNi samples, as depicted in Fig. 5(a-c). The different signs of the slope for Fe<sub>100-x</sub>Ni<sub>x</sub> and Fe<sub>x</sub>Ni<sub>100-x</sub> appear consistent with opposite anti-damping SOTs due to opposite compositional gradients. Yet, we also observe a sizable slope for the compositionally homogeneous Fe<sub>50</sub>Ni<sub>50</sub> sample [Fig. 5(a)].

In the following, we closely inspect the linear slope

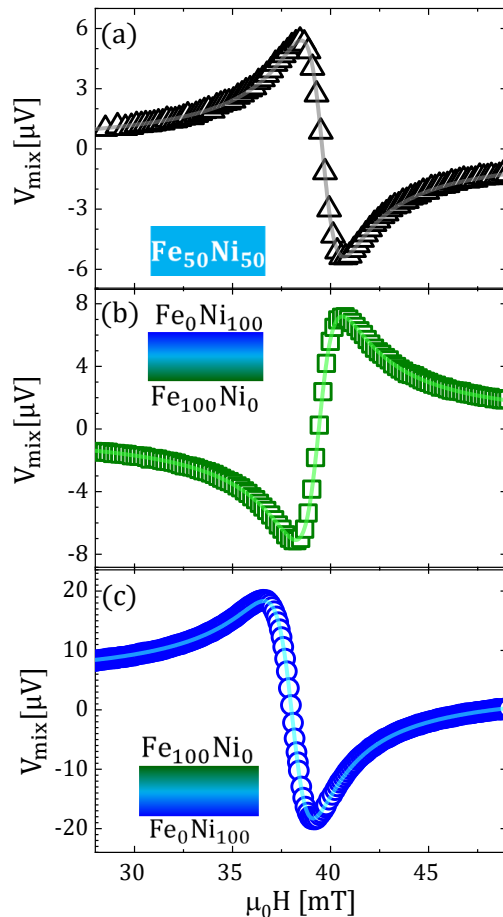


FIG. 4. ST-FMR spectra at  $\phi = 45^\circ$  and frequency  $f = 7$  GHz for (a) Fe<sub>50</sub>Ni<sub>50</sub>, (b) Fe<sub>100-x</sub>Ni<sub>x</sub>, and (c) Fe<sub>x</sub>Ni<sub>100-x</sub>.

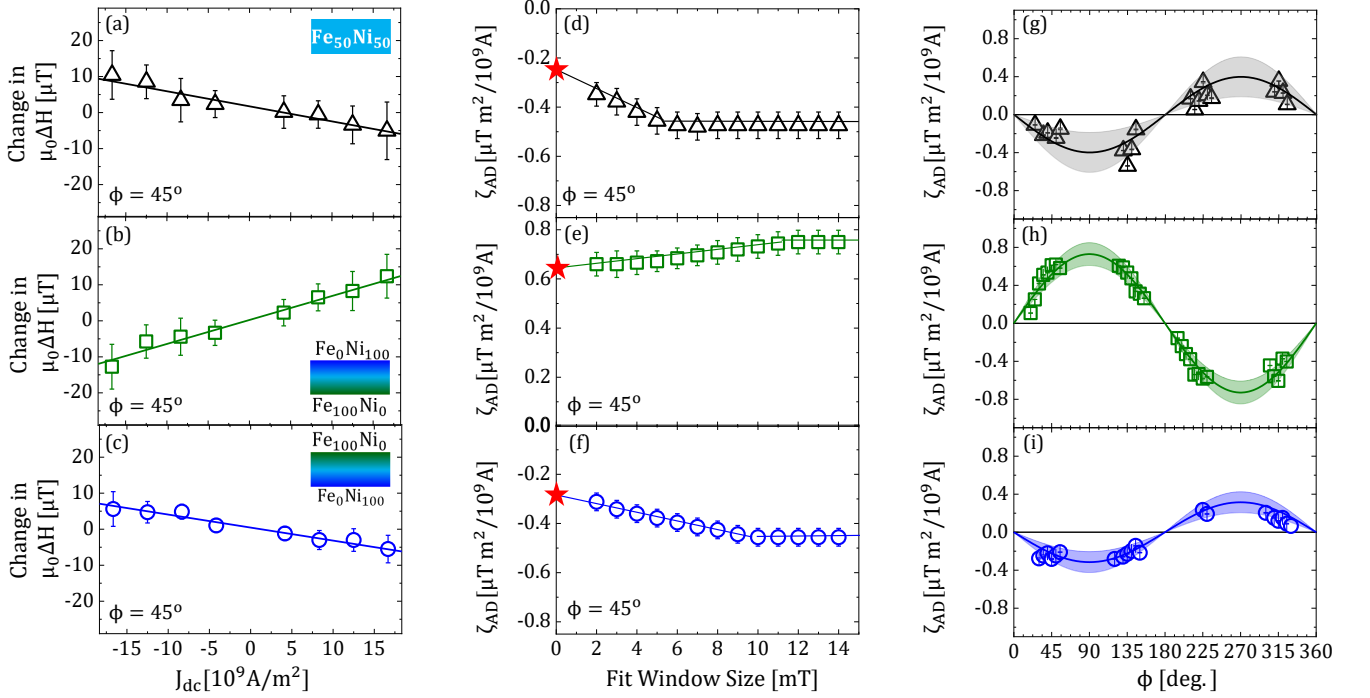


FIG. 5. Left column (a-c): Change in linewidth  $\Delta H$  due to dc bias current density  $J_{dc}$  at fixed in-plane field angle  $\phi = 45^\circ$  for (a)  $\text{Fe}_{50}\text{Ni}_{50}$ , (b)  $\text{Fe}_{100-x}\text{Ni}_x$ , and (c)  $\text{Fe}_x\text{Ni}_{100-x}$ . The dashed line indicates the linear fit to quantify the slope,  $\zeta_{AD}$ . The error bars represent the standard deviation of 20 measurements. Center column (d-f): Change in  $\zeta_{AD}$  with fit window size for (d)  $\text{Fe}_{50}\text{Ni}_{50}$ , (e)  $\text{Fe}_{100-x}\text{Ni}_x$ , and (f)  $\text{Fe}_x\text{Ni}_{100-x}$ . The star at 0  $\mu\text{T}$  indicates  $\zeta_{AD}$  as the fit window size goes to zero, following the protocol in Ref. [49]. Right column (g-i):  $\zeta_{AD}$  plotted against in-plane field angle  $\phi$  for (g)  $\text{Fe}_{50}\text{Ni}_{50}$ , (h)  $\text{Fe}_{100-x}\text{Ni}_x$ , and (i)  $\text{Fe}_x\text{Ni}_{100-x}$ . The solid curve indicates the sinusoid  $\propto \sin \phi$  whose amplitude is the mean of  $\zeta_{AD}/\sin \phi$  over all  $\phi$ , whereas the shaded region indicates  $\pm 1$  standard deviation.

of  $\Delta H$  vs  $J_{dc}$ , denoted as  $\zeta_{AD}$ . Before proceeding to further analysis, we remark that the apparent value of  $\Delta H$  – hence  $\zeta_{AD}$  – can be sensitive to the field range for fitting the ST-FMR spectra [49], even if the spectral fits appear convincing. Indeed, we find that the apparent  $|\zeta_{AD}|$  increases and then saturates with increasing fit window size [Fig. 5(d-f)], in qualitative agreement with Ref. [49]. Following the protocol in Ref. [49], we report the lower-bound value of  $|\zeta_{AD}|$  extrapolated at zero fit window size, indicated as red stars in Fig. 5(d-f).

Figure 5(g-i) summarizes  $\zeta_{AD}$  as a function of the in-plane applied field angle  $\phi$ . The data are adequately captured by the sinusoidal curve  $\propto \sin \phi$ . This observation can be attributed to a dc-induced spin accumulation polarized along the  $\hat{y}$ -axis, which can emerge from a conventional spin Hall effect [6]. In this case, the spin polarization is independent of the magnetization orientation, similar to recent reports of SOTs arising from FMs [57, 58].

Given the  $\sin \phi$  angular dependence, we compute the dimensionless anti-damping SOT efficiency (sometimes called the “effective spin Hall angle”) [48],

$$\theta_{AD} = \frac{2|e|\gamma}{hf} \left[ H_{res} + \frac{M_{eff}}{2} \right] \mu_0 M_s t_{FM} \frac{\zeta_{AD}}{\sin \phi}, \quad (4)$$

where  $\mu_0 M_s = \mu_0 M_{eff} \approx 1.5$  T. As summarized in Table II,

the magnitudes of  $\theta_{AD}$  for the three FeNi samples approach  $\sim 0.1$ . These values of  $\theta_{AD}$  are comparable to those for HM/FM bilayers [2, 3].

We find opposite signs of  $\theta_{AD}$  with opposite compositional gradients<sup>3</sup>. This finding alone might suggest that the anti-damping SOT originates from the steep Fe-Ni compositional gradient. However, this simple scenario is not supported by the quantified values of  $\theta_{AD}$  [Table II]. First,  $|\theta_{AD}|$  is a factor of 2 greater for  $\text{Fe}_{100-x}\text{Ni}_x$  than  $\text{Fe}_x\text{Ni}_{100-x}$ ; reversing the gradient not only reverses the sign of the SOT but also greatly influences its magnitude. More importantly,  $\text{Fe}_{50}\text{Ni}_{50}$

TABLE II. Dimensionless anti-damping SOT efficiency (effective spin Hall angle)  $\theta_{AD}$  quantified from Fig. 5(g-f). The error bars are obtained from the shaded regions in Fig. 5(g-f).

	$\text{Fe}_{50}\text{Ni}_{50}$	$\text{Fe}_{100-x}\text{Ni}_x$	$\text{Fe}_x\text{Ni}_{100-x}$
$\theta_{AD}$	$-0.048 \pm 0.025$	$0.088 \pm 0.016$	$-0.038 \pm 0.013$

<sup>3</sup> Here,  $\theta_{AD} < 0$  ( $> 0$ ) indicates that the polarity of the SOT is consistent with FM/Pt with Pt on top (bottom).

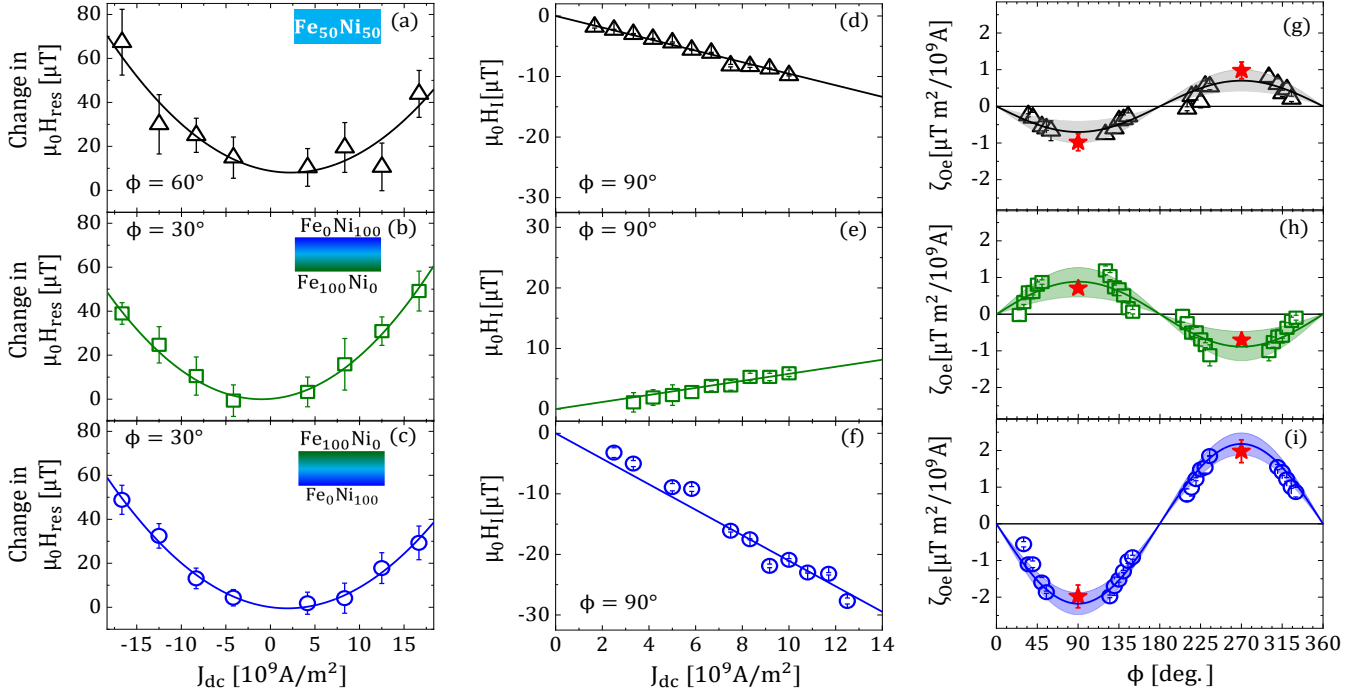


FIG. 6. Left column (a-c): Change in resonance field  $H_{\text{res}}$  with  $J_{\text{dc}}$  for (a)  $\text{Fe}_{50}\text{Ni}_{50}$ , (b)  $\text{Fe}_{100-x}\text{Ni}_x$ , and (c)  $\text{Fe}_x\text{Ni}_{100-x}$ . The dashed curve indicates the quadratic fit of the form  $\beta_{\text{heat}}J_{\text{dc}}^2 + \zeta_{\text{Oe}}J_{\text{dc}}$ , with  $\zeta_{\text{Oe}}$  representing the linear current-induced shift of  $H_{\text{res}}$ . The error bars represent the standard deviation of 20 measurements. Center column (d-f): Linear change in  $\hat{y}$ -oriented current-induced field  $H_I$  with  $J_{\text{dc}}$  from second-order PHE measurements for  $\phi = 90^\circ$  for (d)  $\text{Fe}_{50}\text{Ni}_{50}$ , (e)  $\text{Fe}_{100-x}\text{Ni}_x$ , and (f)  $\text{Fe}_x\text{Ni}_{100-x}$ . Right column (g-i):  $\zeta_{\text{Oe}}$  plotted against in-plane field angle  $\phi$  for (g)  $\text{Fe}_{50}\text{Ni}_{50}$ , (h)  $\text{Fe}_{100-x}\text{Ni}_x$ , and (i)  $\text{Fe}_x\text{Ni}_{100-x}$ . The solid curve indicates the sinusoid  $\propto \sin \phi$  whose amplitude is the mean of  $\zeta_{\text{Oe}}/\sin \phi$  over all  $\phi$ , whereas the shaded region indicates  $\pm 1$  standard deviation. The open symbols indicate  $\zeta_{\text{Oe}}$  from ST-FMR measurements (left column), whereas the red star symbols indicate  $\zeta_{\text{Oe}}^{\text{max}}$  from the PHE measurements (center column) at  $90^\circ$  and  $270^\circ$ .

without any intentional compositional gradient exhibits a sizable  $|\theta_{\text{AD}}|$ , similar in magnitude to the compositionally graded samples.

These observations point to significant anti-damping SOTs with no clear correlation with the intentional compositional gradients. The key question is then: What is the mechanism giving rise to the observed anti-damping SOT? We address this question in the remainder of this article.

## B. Oersted field

The dc bias current (generating the dc anti-damping SOT examined in Sec. IV A) can also generate an in-plane dc Oersted field oriented transverse to the current axis. This Oersted field causes the resonance field  $H_{\text{res}}$  to shift linearly with  $J_{\text{dc}}$  [56, 59]. In reality, as seen in Fig. 6(a-c), we also observe a significant quadratic shift in  $H_{\text{res}}$  with  $J_{\text{dc}}$ , attributed to Joule heating. The overall shift in  $H_{\text{res}}$  with  $J_{\text{dc}}$  is fit with  $\beta_{\text{heat}}J_{\text{dc}}^2 + \zeta_{\text{Oe}}J_{\text{dc}}$ . The linear coefficient  $\zeta_{\text{Oe}}$  captures the shift due to the Oersted field. Figure 6(g-i) summarizes  $\zeta_{\text{Oe}}$  obtained from dc-bias ST-FMR measurements at various values of  $\phi$ .

Around  $\phi \approx 90^\circ$  and  $270^\circ$ , we could not attain sufficient signal-to-noise ratios from dc-bias ST-FMR measurements. To fill in these gaps, the current-induced field  $H_I$ , oriented in-plane and transverse to the current, was measured using the second-order planar Hall effect (PHE) method [13, 60]. These PHE measurements were carried out on 500  $\mu\text{m}$  wide strips, lithographically patterned at the same time as the rectangular ST-FMR strips. This PHE method measures the dc applied field needed to null the planar Hall signal from  $H_I$ ; further details are found in Refs. [13, 60]. Examples of  $H_I$  vs dc current density  $J_{\text{dc}}$  are displayed in Fig. 6(d-f). The observed slope is linear, which implies that the measured response is dominated by the current-induced field, rather than Joule heating. The values of the linear slopes from the PHE measurements are indicated as red stars at  $\phi = 90^\circ$  and  $270^\circ$  in Fig. 6(g-i). They are in good agreement with the  $\phi$  dependence of  $\zeta_{\text{Oe}}$  from the dc bias ST-FMR method.

The combined ST-FMR and PHE results in Fig. 6 are adequately fit with the sinusoid  $\propto \sin \phi$ . This angular dependence is consistent with the symmetry of the dc Oersted field. To represent this  $\hat{y}$ -oriented Oersted field,

we normalize  $\zeta_{\text{Oe}}$  to

$$Z_{\text{Oe}} = \frac{\zeta_{\text{Oe}}}{\sin \phi}. \quad (5)$$

The resulting values of  $Z_{\text{Oe}}$  from the sinusoidal fits of  $\zeta_{\text{Oe}}$  are summarized in Table III.  $\text{Fe}_{100-x}\text{Ni}_x$  and  $\text{Fe}_x\text{Ni}_{100-x}$  with opposite compositional gradients exhibit opposite signs, as intuitively expected. Yet,  $|Z_{\text{Oe}}|$  is a factor of 2 smaller for  $\text{Fe}_{100-x}\text{Ni}_x$  compared to  $\text{Fe}_x\text{Ni}_{100-x}$ . Furthermore,  $\text{Fe}_{50}\text{Ni}_{50}$  with nominally no compositional gradient also exhibits non-negligible  $Z_{\text{Oe}}$  with the same sign as  $\text{Fe}_x\text{Ni}_{100-x}$ .

The maximum possible dc Oersted field – in the most extreme case, with all of the bias current flowing immediately above (or below) the FM layer – is  $|H_{\text{Oe}}^{\text{max}}| = |J_{\text{dc}}|t_{\text{FM}}/2$ . Then, the maximum magnitude of  $Z_{\text{Oe}}$  here is

$$|Z_{\text{Oe}}^{\text{max}}| = \frac{\mu_0 |H_{\text{Oe}}^{\text{max}}|}{|J_{\text{dc}}|} = \frac{\mu_0 t_{\text{FM}}}{2} \approx 6.3 \frac{\mu\text{Tm}^2}{10^9\text{A}}. \quad (6)$$

The magnitudes of  $Z_{\text{Oe}}$  [Table III] are all well below  $|Z_{\text{Oe}}^{\text{max}}|$ . Our results imply that the Oersted field can account for the entire observed current-induced field. In other words, only a small asymmetry in current distribution is needed, with a slight difference in conductivity between the top and bottom portions of the film. For example, the Ni-rich bottom of  $\text{Fe}_x\text{Ni}_{100-x}$  needs to be just  $\approx 30\%$  more conductive than the Fe-rich top. Moreover,  $\text{Fe}_{50}\text{Ni}_{50}$  requires only  $\approx 10\%$  asymmetry in conductivity. Even though  $\text{Fe}_{50}\text{Ni}_{50}$  has no intentional symmetry breaking, the slight conductivity asymmetry can plausibly arise, e.g., with a subtle difference between the top and bottom interfaces of  $\text{Fe}_{50}\text{Ni}_{50}$ .

Some portion of the current-induced field possibly originates from spin-orbit effects (i.e., “field-like” SOT) [3, 13, 60]. However, we emphasize that an uncompensated Oersted field adequately explains our observation, without invoking any additional spin-orbit field. It is natural to deduce that the field-like SOT is likely much weaker than the classical Oersted field torque in the FeNi samples examined here.

### C. Current-induced torques vs nominal compositional gradient

To gain a broader perspective on the current-induced torques, we compare how the anti-damping SOT and

TABLE III. Current-induced field (assumed to be the Oersted field) per unit current density  $Z_{\text{Oe}}$ . The error bars are obtained from the shaded regions in Fig. 6(g-f).

	$\text{Fe}_{50}\text{Ni}_{50}$	$\text{Fe}_{100-x}\text{Ni}_x$	$\text{Fe}_x\text{Ni}_{100-x}$
$Z_{\text{Oe}} \left( \frac{\mu\text{Tm}^2}{10^9\text{A}} \right)$	$-0.70 \pm 0.06$	$0.87 \pm 0.06$	$-2.18 \pm 0.04$

the Oersted field depend on the nominal compositional gradient in Fig. 7. The anti-damping SOT efficiency  $\theta_{\text{AD}}$  exhibits a nonlinear trend [Fig. 7(a)]. In contrast, the Oersted field parameter  $Z_{\text{Oe}}$  appears to scale linearly with the compositional gradient [Fig. 7(b)], albeit with an offset yielding nonzero  $Z_{\text{Oe}}$  for  $\text{Fe}_{50}\text{Ni}_{50}$ . As discussed in Sec. IV B, the linear scaling for  $Z_{\text{Oe}}$  is readily explained by an asymmetric current distribution that approximately tracks the compositional gradient. Yet, the origin of the anti-damping SOT is far less clear from the results in Fig. 7 alone.

Nevertheless, it is instructive to re-emphasize key points from the results in Fig. 7. First and foremost, the intentional compositional gradient cannot fully account for the observed anti-damping SOT. Similarly, an uncompensated spin accumulation from any current imbalance (i.e., conductivity asymmetry from compositional asymmetry) is not the primary contribution to the anti-damping SOT; if it were,  $\theta_{\text{AD}}$  would have to show a similar scaling as the  $Z_{\text{Oe}}$ . The above points suggest that we must consider an alternative source of symmetry breaking for the anti-damping SOT.

## V. DEPTH-RESOLVED PROPERTIES

We now examine the origin of the anti-damping SOT without any clear scaling with the intentional Fe-Ni compositional gradient. We posit two possibilities of *unintentional* symmetry breaking that can generate the unexpected SOT:

First, the actual compositional profile along the film thickness might be significantly different from the intended one illustrated in Fig. 2. For instance, the nominally homogeneous  $\text{Fe}_{50}\text{Ni}_{50}$  film might exhibit a significant compositional gradient [61] due to phase segregation. Alternatively, atomic intermixing during deposition can lead to non-negligible gradients at film interfaces. In Sec. V A, we present spin-polarized neutron reflectometry (PNR) measurements that verify the compositional and magnetic depth profiles of the three FeNi films.

Second, a change in the lattice parameter – i.e., a strain gradient – along the FM thickness might provide the required symmetry breaking for the SOT. Such a strain gradient might arise during film growth (e.g., governed by mismatch in lattice parameters among the different film layers). Indeed, previous experiments have suggest strain gradients as a possible mechanism for SOTs in nominally homogeneous FMs [25], although no direct evidence has been presented for such strain gradients. In Sec. V B, we directly quantify the change of the lattice parameter along the film thickness through grazing-incidence x-ray diffraction (GI-XRD).

PNR and GI-XRD are *non-destructive* methods, enabling depth-resolved characterization without any irreversible sample damage. This is in contrast to cross-sectional transmission electron microscopy, in which the



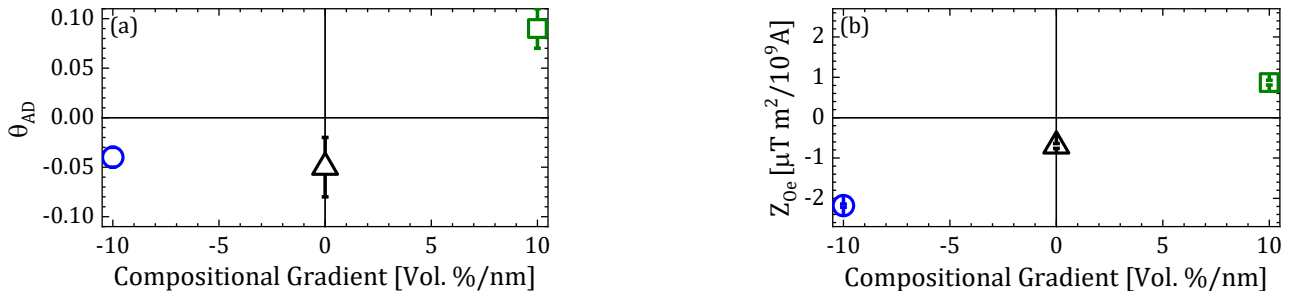


FIG. 7. Compositional gradient dependence of (a) anti-damping SOT efficiency  $\theta_{AD}$  and (b) current-induced field per unit current density  $Z_{Oe}$ . The error bars indicate  $\pm 1$  standard deviation computed over the full angular dependence (shaded region in Figs. 5(g-i) and 6(g-i)).

milling for sample preparation can irreversibly relax the built-in strain in the film. Our PNR and GI-XRD measurements were performed on unpatterned films with lateral dimensions  $> 2 \times 2$  cm<sup>2</sup>. Some films were subjected to a process that emulated the heating during the microfabrication of the patterned samples for the SOT experiments; the films were coated with photoresist, baked, and ion-milled for the same duration as the patterned samples in Sec. IV. The films with and without heating exhibit no systematic difference in the PNR and GI-XRD results. In the following, we present PNR and GI-XRD results from the “heated” samples.

### A. Compositional gradient

To verify the compositional and magnetic gradients, PNR was performed using the Polref instrument at the ISIS Neutron and Muon Source. The probed films were grown on thermally-oxidized Si and (0001)-oriented sapphire substrates. The results were essentially identical irrespective of the substrate; here, we show PNR results for the films on sapphire substrates, which provide better nuclear scattering length density contrast with the film. The measurements were conducted under an in-plane applied magnetic field of 0.7 T, sufficient to saturate the samples. The neutron beam was spin-polarized parallel or antiparallel to the field, and the corresponding reflectivity cross sections ( $R^+$  and  $R^-$ ) were measured as a function of the perpendicular scattering wavevector  $Q_z$ . The obtained PNR data are shown in Fig. 8(a-c).

PNR depends on the depth profiles of the nuclear scattering length density  $\rho_N$  and magnetic scattering length density  $\rho_M$ . We use the Refl1D package [62] to fit the PNR data [Fig. 8(a-c)] and extract the profiles of the composition ( $\propto \rho_N$  in Fig. 8(d-f)) and net in-plane magnetization ( $\propto \rho_M$  in Fig. 8(g-i)) along the vertical coordinate  $z$ . In modeling each sample, the FM layer is represented by five equal-thickness sections

with equally rough interfaces to approximate a smooth gradient of alloy composition and magnetization. The fitting reproduces the PNR results well, as seen in Fig. 8(a-c). The derived depth profiles, as summarized in Fig. 8(d-h), are also in good agreement with the nominal film stack structures [Fig. 2]. The only major exception is that the top Ti layer is partially oxidized, which is reasonable as the films are exposed to ambient air. The parameters in our modeling are summarized in Table IV.

The nominally asymmetric  $Fe_{100-x}Ni_x$  and  $Fe_xNi_{100-x}$  samples show clear linear slopes in  $\rho_N$  [Fig. 8(e,f)] and  $\rho_M$  [Fig. 8(h,i)] with opposite direction within the FM layer. The direction of the slope in  $\rho_N$  agrees with the intended compositional profile. Similarly, the slope in  $\rho_M$  is also consistent with the compositional gradient, which naturally leads to a magnetic gradient. Given the greater magnetism of Fe compared to Ni, the Fe-rich bottom of  $Fe_{100-x}Ni_x$  leads to larger  $\rho_M$  at lower  $z$ . Indeed, the linearly extrapolated values of  $\rho_M$  at the top ( $z = 10$  nm) and bottom ( $z = 0$  nm) interfaces agree well with the tabulated values of  $\approx 5 \times 10^{-4}$  nm<sup>-2</sup> for Fe and  $\approx 1.5 \times 10^{-4}$  nm<sup>-2</sup> for Ni [63] – further giving credence to the quantitative accuracy of our PNR fit results.

The PNR results for  $Fe_{50}Ni_{50}$  are also largely consistent with the intended film stack structure, showing a nearly uniform depth profile within bulk of the FM layer. Although the gradients of  $\rho_N$  and  $\rho_M$  are in fact nonzero in the bulk of  $Fe_{50}Ni_{50}$  [Table IV], they are tiny – more than an order of magnitude smaller than the gradients in  $Fe_{100-x}Ni_x$  and  $Fe_xNi_{100-x}$ . Thus, the unintentional bulk compositional or magnetic gradient is highly unlikely to be the primary source of asymmetry for the SOT in  $Fe_{50}Ni_{50}$ .

We do find non-negligible asymmetry between the bottom Cu/ $Fe_{50}Ni_{50}$  and top  $Fe_{50}Ni_{50}$ /Cu interfaces. In particular, the top interface exhibits shallower gradients in both  $\rho_N$  and  $\rho_M$ , which can arise due to greater atomic intermixing [65]. Such asymmetry between the interfaces has been reported to give rise to an uncompensated

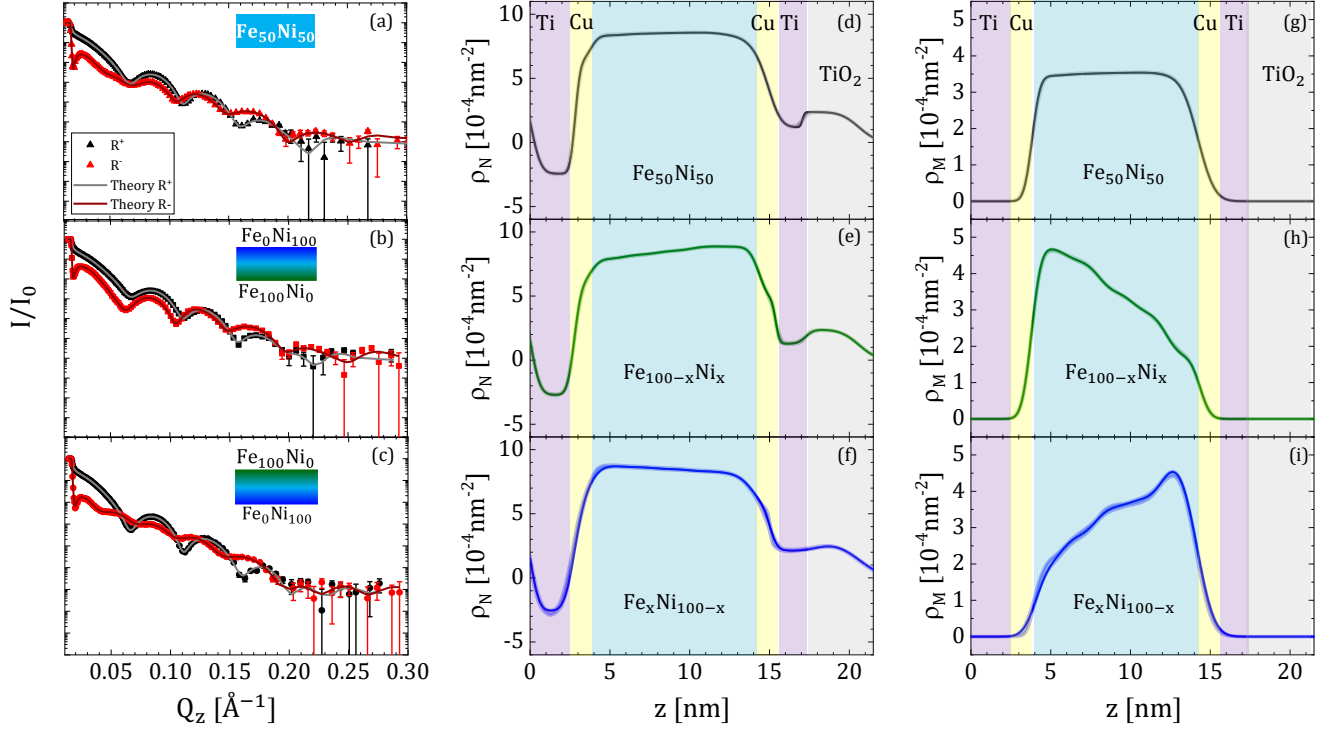


FIG. 8. Left column (a-c): Normalized reflectivity in reciprocal space for polarized neutrons spin up,  $R^+$ , or spin down,  $R^-$ , (closed symbols) for (a)  $\text{Fe}_{50}\text{Ni}_{50}$ , (b)  $\text{Fe}_{100-x}\text{Ni}_x$ , (c)  $\text{Fe}_x\text{Ni}_{100-x}$ . Theoretical fits solid line grey ( $R^+$ ), maroon ( $R^-$ ). Center column (d-f): Nuclear scattering length density  $\rho_N$  with film thickness  $z$  for (d)  $\text{Fe}_{50}\text{Ni}_{50}$ , (e)  $\text{Fe}_{100-x}\text{Ni}_x$ , and (f)  $\text{Fe}_x\text{Ni}_{100-x}$ . Right column (g-i): magnetic scattering length density  $\rho_M$  and corresponding magnetization  $M$  ( $1 \text{ kA/m} = 2.91 \times 10^{-7} \text{ nm}^{-2}$ ) with film thickness  $z$ , for (g)  $\text{Fe}_{50}\text{Ni}_{50}$  (h)  $\text{Fe}_{100-x}\text{Ni}_x$ , and (i)  $\text{Fe}_x\text{Ni}_{100-x}$ . Error bars represent  $\pm 1$  standard deviation. Shaded bands indicate the 95% confidence bands of the best-fit depth profiles, determined by Markov chain Monte Carlo calculations.

SOT and Dzyaloshinskii-Moriya interaction in sub-nm thin FM sandwiched between Pt [66, 67]. However, we find it difficult to justify that the asymmetric interfaces sufficiently account for the sizable SOT in  $\text{Fe}_{50}\text{Ni}_{50}$ . The large FM thickness of 10 nm would likely make it difficult for the uncompensated interfacial

spin accumulations to generate a sizable torque. More crucially, as shown in Fig. 8, the overall compositional and magnetic asymmetries are clearly much greater in the graded  $\text{Fe}_{100-x}\text{Ni}_x$  and  $\text{Fe}_x\text{Ni}_{100-x}$  than in  $\text{Fe}_{50}\text{Ni}_{50}$ . It is hence doubtful that the asymmetries apparent in the PNR results [Fig. 8] alone are responsible for the SOT in  $\text{Fe}_{50}\text{Ni}_{50}$ . Rather than a mechanism originating from the *compositional* profile (and, by association, magnetic profile) in the bulk or at the interfaces, we suspect *structural* asymmetry to play a critical role, particularly in  $\text{Fe}_{50}\text{Ni}_{50}$ .

TABLE IV. Calculated theoretical scattering length densities for various compositions and densities extracted from Fig. 9, for comparison with Fig. 8.

	$\text{Fe}_{50}\text{Ni}_{50}$	$\text{Fe}_{100-x}\text{Ni}_x$	$\text{Fe}_x\text{Ni}_{100-x}$
atomic composition	$\text{Fe}_{48}\text{Ni}_{52}$	Ni	Fe
$a_{\text{fcc}}$ (nm)	0.3557	0.3536	0.3560
Top $\rho$ ( $\text{g}/\text{cm}^3$ )	8.460	8.818	8.22
$\rho_N$ ( $10^{-4} \text{ nm}^{-2}$ )	8.791	9.319	8.377
$\mu_0 M_s$ (T) [64]	1.51	0.45	2.05
$\rho_M$ ( $10^{-4} \text{ nm}^{-2}$ )	3.723	1.15	4.90
atomic composition	$\text{Fe}_{48}\text{Ni}_{52}$	Fe	Ni
$a_{\text{fcc}}$ (nm)	0.3573	0.3546	0.3560
Bot. $\rho$ ( $\text{g}/\text{cm}^3$ )	8.347	8.319	8.640
$\rho_N$ ( $10^{-4} \text{ nm}^{-2}$ )	8.673	8.478	9.131
$\mu_0 M_s$ (T) [64]	1.51	2.05	0.45
$\rho_M$ ( $10^{-4} \text{ nm}^{-2}$ )	3.673	4.96	1.13
$\chi^2$ of fit	1.165(55)	1.090(18)	1.217(69)

## B. Strain gradient

We employed GI-XRD to evaluate the lattice parameter as a function of depth. Unlike conventional XRD where the Bragg diffraction angle  $2\theta$  is scanned and the incident angle  $\omega_i$  is set to  $\theta$  (i.e., the incident and diffracted beams are symmetric), GI-XRD is performed by scanning  $2\theta$  while setting  $\omega_i$  to a much smaller value, typically around  $\sim 1^\circ$  (i.e., the incident and diffracted beams are asymmetric). While conventional XRD is primarily sensitive to crystal planes parallel to the sample surface, GI-XRD can pick up diffraction from crystal

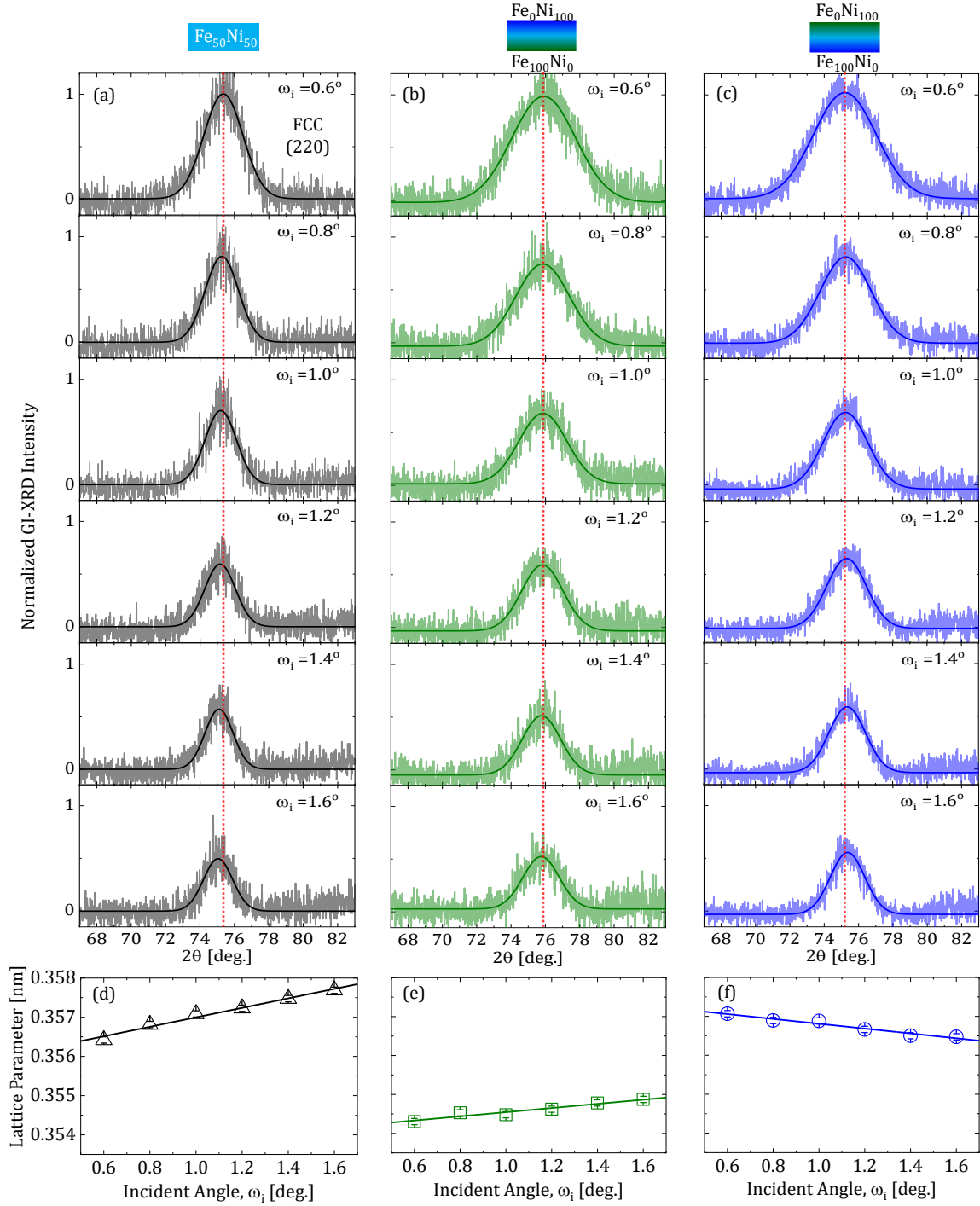


FIG. 9. (Bottom Panel) (a-c) Grazing-incidence XRD spectra, with the shift from refraction corrected (see Appendix B for details), from incident angle  $\omega_i = 0.60^\circ$  (top side of the FM) to  $\omega_i = 1.60^\circ$  (bottom side of the FM) for (a)  $\text{Fe}_{50}\text{Ni}_{50}$ , (b)  $\text{Fe}_{100-x}\text{Ni}_x$ , and (c)  $\text{Fe}_x\text{Ni}_{100-x}$ . The intensity is normalized by the amplitude of the Gaussian fit peak at  $\omega_i = 0.60^\circ$ . (d-f) Change in lattice parameter with  $\omega_i$  for (d)  $\text{Fe}_{50}\text{Ni}_{50}$ , (e)  $\text{Fe}_{100-x}\text{Ni}_x$ , and (f)  $\text{Fe}_x\text{Ni}_{100-x}$ . The error bars, propagated from the uncertainty of  $\approx 0.02^\circ$  in the peak center in (a-c), are of the order of the symbol size.

planes tilted from the sample surface.

When  $\omega_i$  is below the critical angle in x-ray reflectometry ( $(2\theta_c)/2 \approx 0.4^\circ$  here), most of the x-ray beam does not penetrate into the sample. Increasing

$\omega_i$  beyond the critical angle permits the x-ray beam to penetrate deeper into the film, thereby yielding a diffraction signal for different depths along the film thickness. At  $\omega_i \gtrsim 1.8^\circ$ , the diffraction signal is

dominated by the substrate plane, Si(311), indicating that the beam penetrates through the film. Therefore, we focus on GI-XRD measurements at  $\omega_i$  between  $0.6^\circ$  and  $1.6^\circ$ , with an  $\omega_i$  step size of  $0.2^\circ$ , to acquire the diffraction response primarily from the 10 nm thick FM.

We begin by discussing results from  $\text{Fe}_{50}\text{Ni}_{50}$ , for which GI-XRD provides the most useful insight into the symmetry breaking presumably underlying the anti-damping SOT. As shown in Fig. 9(a), we observe a pronounced diffraction peak around  $2\theta \approx 75^\circ$ , attributed to the (220) plane of face-centered cubic (fcc)  $\text{Fe}_{50}\text{Ni}_{50}$  [64]. We do not observe a diffraction peak around  $2\theta \approx 44^\circ$  that would arise from the presence of an Fe-rich body-centered cubic (bcc) phase [41]. Thus, our GI-XRD results corroborate a homogeneous crystal phase across the thickness of  $\text{Fe}_{50}\text{Ni}_{50}$ .

Despite the homogeneous crystal phase in  $\text{Fe}_{50}\text{Ni}_{50}$ , a systematic linear shift in the position of the diffraction peak [Fig. 9(a)] is observed. We remark that the refraction of the x-ray beam can cause the diffraction peak to shift [68, 69], but this refraction-induced peak shift is readily computed, as explained in Appendix B. In Fig. 9, the GI-XRD results are shown with the refraction-induced peak shift subtracted. By applying Bragg’s law, we obtain a lattice parameter of  $\approx 0.3565$  nm near the top of the  $\text{Fe}_{50}\text{Ni}_{50}$  film ( $\omega_i = 0.6^\circ$ ), which is close to the bulk  $\text{Fe}_{50}\text{Ni}_{50}$  lattice parameter of  $\approx 0.356$  nm. We find a larger lattice parameter of  $\approx 0.3576$  nm near the bottom of the film ( $\omega_i = 1.6^\circ$ ), which is closer to the bulk lattice parameter  $\approx 0.361$  nm of fcc Cu<sup>4</sup>. Our observation is consistent with the  $\text{Fe}_{50}\text{Ni}_{50}$  lattice strained on the bottom to match the underlying Cu seed layer and progressively relaxing toward the top. Assuming that  $\omega_i = 0.6 - 1.6^\circ$  primarily probes the film as explained previously, we estimate a linear strain gradient of  $\sim 0.3\%$  over the  $\text{Fe}_{50}\text{Ni}_{50}$  thickness of 10 nm. Moreover, this strain gradient is qualitatively consistent with the slight density gradient in  $\text{Fe}_{50}\text{Ni}_{50}$  seen using PNR [Tab. IV].

We observe similar gradients for an as-grown  $\text{Fe}_{50}\text{Ni}_{50}$  sample and the  $\text{Fe}_{50}\text{Ni}_{50}$  sample subjected to heating and milling that emulate the microfabrication steps – corroborating the notion that the strain gradient arises during film growth, rather than any post processes. This growth-induced residual strain gradient appears to be the most plausible symmetry-breaking mechanism that accounts for the sizable anti-damping SOT in  $\text{Fe}_{50}\text{Ni}_{50}$ . Our GI-XRD work demonstrates that a strain gradient provides the needed symmetry breaking for the SOT, even in a single-layer FM without any significant compositional asymmetry.

The compositionally graded  $\text{Fe}_{100-x}\text{Ni}_x$  and  $\text{Fe}_x\text{Ni}_{100-x}$  samples exhibit both bcc (110) and fcc (220) diffraction peaks. The intentional compositional gradients lead to mixed crystalline phases, with Fe-rich

regions being bcc and Ni-rich regions being fcc [64]. However, the signal-to-noise ratio of the bcc (110) peak is insufficient for precisely quantifying the lattice parameter. Therefore, we focus on analyzing the fcc (220) diffraction peak [Fig. 9(b,c)]. We observe strain gradients of  $\sim 0.15\%$  of opposite polarity in  $\text{Fe}_{100-x}\text{Ni}_x$  and  $\text{Fe}_x\text{Ni}_{100-x}$  [Fig. 9(e,f)]. This trend is qualitatively reasonable: the lattice parameter towards the top of  $\text{Fe}_{100-x}\text{Ni}_x$  approaches that of Ni (0.353 nm), whereas the lattice parameter towards the top of  $\text{Fe}_x\text{Ni}_{100-x}$  approaches that of Fe-rich fcc FeNi alloy (0.360 nm) [64].

## VI. DISCUSSION

It is instructive to consider how the strain gradient permits uncompensated current-induced spin accumulations that exert torques on the magnetization. A local strain may sufficiently modify the electronic band structure, and hence the intrinsic spin Hall effect, as corroborated by studies of SOTs in films on piezoelectric and bendable substrates [70, 71]. In our case with FM films on rigid substrates, a built-in residual strain gradient can establish a gradient of the intrinsic spin Hall effect. While a uniform spin Hall effect in the FM would yield a net zero non-equilibrium spin accumulation [57], the strain-induced *graded* spin Hall effect can generate a net nonzero spin accumulation throughout the FM thickness. Alternatively, the strain gradient may produce a graded orbital Hall effect [72], yielding a net orbital accumulation that is converted to a spin accumulation via spin-orbit coupling [73]. This is an intriguing possibility, given that the lattice strain should couple more directly to the orbital (rather than spin) degree of freedom in the FM.

In  $\text{Fe}_{100-x}\text{Ni}_x$  and  $\text{Fe}_x\text{Ni}_{100-x}$ , the steep compositional gradients may still be the primary source of asymmetry for the anti-damping SOT. Yet, as summarized in Fig 7(a) and Table II,  $\text{Fe}_{100-x}\text{Ni}_x$  with a “positive” strain gradient [Fig. 9(e)] exhibits a factor of 2 greater anti-damping SOT than  $\text{Fe}_x\text{Ni}_{100-x}$  with a “negative” strain gradient [Fig. 9(f)]. This observation suggests that a vertical strain gradient of a certain polarity may be more effective in enhancing the anti-damping SOT, although the reason for this is yet unclear. For further enhancement, the strain gradient may be deliberately tuned by varying the film thickness, the sputtering gas pressure, the substrate, or the seed layer composition. Our present study indicates that asymmetry in chemical composition is not the only route to SOTs. Rather, asymmetry in microstructure may be another effective approach to enhance SOTs.

One remaining mystery is the polarity of the anti-damping SOT in  $\text{Fe}_{50}\text{Ni}_{50}$ . In particular,  $\text{Fe}_{50}\text{Ni}_{50}$  and  $\text{Fe}_{100-x}\text{Ni}_x$  share the same strain gradient direction [Fig. 9(d,e)], but they exhibit opposite anti-damping SOT polarities [Fig. 7]. This discrepancy suggests the need for a more nuanced explanation, perhaps

<sup>4</sup> The ultrathin Cu layer itself is likely strained, so its lattice parameter is not necessarily equal to the bulk value

involving the qualitative structural difference between the homogeneous  $\text{Fe}_{50}\text{Ni}_{50}$  alloy (purely fcc) and the graded  $\text{Fe}_{100-x}\text{Ni}_x$  alloy (mixed bcc + fcc phases). We may not be able to make a straightforward comparison of anti-damping SOT mechanisms between these two distinct alloys. Further studies are warranted to uncover the full interplay of compositional and strain gradients in FMs.

## VII. SUMMARY

Our work demonstrates that low damping and a sizable SOT can coexist in symmetry-broken single-layer polycrystalline FMs. In 10 nm thick FeNi with and without intentional compositional gradients, we have quantified effective damping parameters of  $\alpha_{\text{eff}} < 5 \times 10^{-3}$  (lower than that in permalloy) and anti-damping SOT efficiencies approaching  $|\theta_{\text{AD}}|$  of order 0.1 (on par with oft-studied HM/FM bilayers). These findings illuminate a new path toward developing low-loss Type-Y spintronic memories and oscillators. Moreover, the sizable SOT in these single-layer all-3d FMs supports the recent notion that the HM in HM/FM bilayers is not the sole source of current-induced spin accumulation – but rather the FM can host its own current-induced spin accumulation that generates a “self torque” within itself [5, 7, 57].

Another notable implication is that we may not necessarily need compositional asymmetry to attain a sizable SOT. In particular, a built-in *strain gradient* in  $\text{Fe}_{50}\text{Ni}_{50}$  here may contribute to an anti-damping SOT comparable to that from compositional gradients. Such a strain gradient within the FM bulk could possibly explain SOTs reported in compositionally symmetric single-layer FMs [74, 75]. Future studies may deliberately engineer the strain gradient to enhance the SOT efficiency. Our work motivates further endeavors to uncover the fundamental impacts of compositional and strain gradients on spintronic (and potentially orbitronic) phenomena for energy-efficient nanomagnetic devices.

## ACKNOWLEDGMENTS

R.E.M., J.L.J., and S.E. were supported by the National Science Foundation under Grant No. ECCS-2144333. D.A.S. and W.C.T. were supported by the National Science Foundation under Grant No. DMR-2003914. Y.L. was supported by the Air Force Office of Scientific Research (AFOSR) under Grant No. FA9550-21-1-0365. P.P.B. was supported by an NRC RAP award. We thank Vivek P. Amin for helpful discussions. We thank the ISIS Neutron and Muon Source for the provision of beamtime. Raw PNR data from the Polref instrument can be accessed at <https://doi.org/10.5286/ISIS.E.RB2210102>.

The authors contributed to the following components of this work. Conceptualization: S.E. Project

management: R.E.M and S.E. Film growth: R.E.M. and S.W. In-plane FMR: R.E.M. and S.W. Out-of-plane FMR: P.N., B.N., and T.M. Microfabrication: R.E.M., S.W., D.A.S, and Y.L. ST-FMR: R.E.M. and S.E. Second-order PHE: R.E.M., J.L.J., W.C.T., and S.E. PNR: P.P.B., A.J.G., C.J.K., and A.J.C. GI-XRD: R.E.M., J.Z., F.M.M., and S.E. Initial draft: R.E.M., P.P.B., A.J.G., and S.E. Review of the initial draft: all. Final draft: R.E.M., S.W., P.P.B., A.G.J., T.M., and S.E.

## Appendix A: Spin-Torque FMR Methods

For ST-FMR measurements, rectangular strips were patterned by photolithography and Ar ion milling. An additional layer of photolithography and liftoff was performed to contact these strips with electrodes, consisting of Ti(3 nm)/Cu(100 nm)/Pt(2 nm). A ground-signal-ground probe was used to apply a 7 GHz microwave current at a power of +8 dBm. An in-plane applied field is swept at in-plane angle  $\phi$  with respect to the current axis. The microwave current generates oscillatory torques that drive the magnetization about the field, leading to a change in the anisotropic magnetoresistance at the frequency of 7 GHz. The mixing of the microwave current and oscillating magnetoresistance produces a rectified voltage signal  $V_{\text{mix}}$  [48]. We detected  $V_{\text{mix}}$  using a lock-in amplifier with a reference frequency of 1777.77 Hz for amplitude modulation of the microwave current. Figure 4 shows examples of ST-FMR spectra, obtained by acquiring  $V_{\text{mix}}$  while sweeping the in-plane applied field  $H$ . These spectra are fit with the generalized Lorentzian of the form

$$V_{\text{mix}} = \frac{\Delta H}{\Delta H^2 + (H - H_{\text{res}})^2} [S\Delta H + A(H - H_{\text{res}})], \quad (\text{A1})$$

where  $S$  and  $A$  are the coefficients for the symmetric and antisymmetric parts of the Lorentzian. From Eq. A1, we quantify the resonance field  $H_{\text{res}}$  and the half-width-at-half-maximum FMR linewidth  $\Delta H$ .

Our experimental setup limits the maximum dc current amplitude to 10 mA. By taking the width 50  $\mu\text{m}$  and conductive thickness 12 nm (i.e., accounting for the FeNi layer and the Cu seed and capping layers, while ignoring the highly resistive Ti layers), we have an average current density of up to  $|J_{\text{dc}}| = 17 \times 10^9 \text{ A/m}^2$ . At each value of  $J_{\text{dc}}$ , we averaged 20 measurements to quantify  $\Delta H$  and  $H_{\text{res}}$ .

## Appendix B: GI-XRD Peak Shift due to Refraction

In GI-XRD, a diffraction peak shifts with the incident angle  $\omega_i$  due to the refraction of the x-ray beam [68, 69]. The GI-XRD spectra displayed in Fig. 9 account for this effect – i.e., the refraction-induced shift  $\Delta 2\theta$  is subtracted

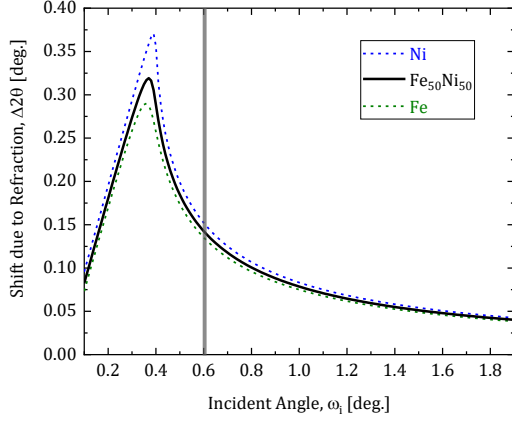


FIG. 10. Diffraction peak shift  $\Delta 2\theta$  due to refraction as a function of incident angle  $\omega_i$ , computed with Eq. B1

from  $2\theta$ . The shift  $\Delta 2\theta$  as a function of  $\omega_i$  is computed

with [68]

$$\Delta 2\theta = \omega_i - \frac{1}{\sqrt{2}} \sqrt{[(\omega_i^2 - 2\delta)^2 + 4\beta^2]^{1/2} + (\omega_i^2 - 2\delta)^2}, \quad (\text{B1})$$

where  $\delta$  and  $\beta$  are the dispersive and absorptive components, respectively, of the refractive index of the film material,  $r = 1 - \delta - i\beta$ . The values of  $\delta$  and  $\beta$ , which depend on the material composition and density, can be readily found from databases and calculators available online [76]. For example, for  $\text{Fe}_{50}\text{Ni}_{50}$  with density  $8.40 \text{ g/cm}^3$  [Table IV], we have  $\delta = 2.3 \times 10^{-5}$  and  $\beta = 2 \times 10^{-6}$  at Cu  $K\alpha 1$  x-ray wavelength  $0.15406 \text{ nm}$  (or photon energy  $8048 \text{ eV}$ ). The resulting refraction-induced GI-XRD peak shift  $\Delta 2\theta$  is shown in Fig. 10.

The exact calculation of  $\Delta 2\theta$  would be much more difficult for compositionally graded films because, strictly speaking,  $\delta$  and  $\beta$  would depend on the position along the film thickness. Fortunately, as shown in Fig. 10,  $\text{Fe}_{50}\text{Ni}_{50}$ , Fe, and Ni exhibit similar values of  $\Delta 2\theta$  in the incident angle range of interest to us ( $\omega_i > 0.6^\circ$ ). For example, at  $\omega_i = 0.6^\circ$ , we have  $\Delta 2\theta = 0.143^\circ$  for  $\text{Fe}_{50}\text{Ni}_{50}$ ;  $\Delta 2\theta$  deviates from that value by only  $< 0.010^\circ$  for Fe and Ni. As a good approximation,  $\Delta 2\theta$  computed for  $\text{Fe}_{50}\text{Ni}_{50}$  is applied to all three materials examined in this study.

- 
- [1] A. Hirohata, K. Yamada, Y. Nakatani, L. Prejbeanu, B. Diény, P. Pirro, and B. Hillebrands, *Journal of Magnetism and Magnetic Materials* **509**, 166711 (2020).
- [2] Q. Shao, P. Li, L. Liu, H. Yang, S. Fukami, A. Razavi, H. Wu, K. Wang, F. Freimuth, Y. Mokrousov, M. D. Stiles, S. Emori, A. Hoffmann, J. Akerman, K. Roy, J.-P. Wang, S.-H. Yang, K. Garellob, and W. Zhang, *IEEE Transactions on Magnetism*, 1 (2021).
- [3] A. Manchon, J. Železný, I. M. Miron, T. Jungwirth, J. Sinova, A. Thiaville, K. Garello, and P. Gambardella, *Reviews of Modern Physics* **91**, 035004 (2019).
- [4] S. Fukami, T. Anekawa, C. Zhang, and H. Ohno, *Nature Nanotechnology* **11**, 621 (2016).
- [5] A. Davidson, V. P. Amin, W. S. Aljuaid, P. M. Haney, and X. Fan, *Physics Letters A* **384**, 126228 (2020).
- [6] J. Sinova, S. O. Valenzuela, J. Wunderlich, C. H. Back, and T. Jungwirth, *Reviews of Modern Physics* **87**, 1213 (2015).
- [7] K. W. Kim and K. J. Lee, *Physical Review Letters* **125**, 207205 (2020).
- [8] T. Taniguchi, J. Grollier, and M. D. Stiles, *Physical Review Applied* **3**, 044001 (2015).
- [9] S. heon C. Baek, V. P. Amin, Y.-W. Oh, G. Go, S.-J. Lee, G.-H. Lee, K.-J. Kim, M. D. Stiles, B.-G. Park, and K.-J. Lee, *Nature Materials* **17**, 509 (2018).
- [10] T. C. Chuang, C. F. Pai, and S. Y. Huang, *Physical Review Applied* **11**, 061005 (2019).
- [11] E. A. Montoya, X. Pei, and I. N. Krivorotov, arXiv:2401.05006 (2024).
- [12] P. M. Haney, H.-W. Lee, K.-J. Lee, A. Manchon, and M. D. Stiles, *Physical Review B* **87**, 174411 (2013).
- [13] X. Fan, H. Celik, J. Wu, C. Ni, K.-J. Lee, V. O. Lorenz, and J. Q. Xiao, *Nature Communications* **5**, 3042 (2014).
- [14] Y. Tserkovnyak, A. Brataas, G. E. W. Bauer, and B. I. Halperin, *Reviews of Modern Physics* **77**, 1375 (2005).
- [15] R. McMichael and P. Krivosik, *IEEE Transactions on Magnetism* **40**, 2 (2004).
- [16] L. Zhu, D. C. Ralph, and R. A. Buhrman, *Physical Review Letters* **123**, 057203 (2019).
- [17] L. Fallarino, B. Kirby, and E. Fullerton, *Journal of Physics D: Applied Physics* **54**, 303002 (2021).
- [18] M. Tang, K. Shen, S. Xu, H. Yang, S. Hu, W. Lü, C. Li, M. Li, Z. Yuan, S. J. Pennycook, K. Xia, A. Manchon, S. Zhou, and X. Qiu, *Advanced Materials* **32**, 2002607 (2020).
- [19] L. Liu, J. Yu, R. González-Hernández, C. Li, J. Deng, W. Lin, C. Zhou, T. Zhou, J. Zhou, H. Wang, R. Guo, H. Y. Yoong, G. M. Chow, X. Han, B. Dupé, J. Železný, J. Sinova, and J. Chen, *Physical Review B* **101**, 220402 (2020).
- [20] Y. Tao, C. Sun, W. Li, L. Yang, F. Jin, Y. Hui, H. Li, X. Wang, and K. Dong, *Applied Physics Letters* **120**, 102405 (2022).
- [21] L. Zhu, X. S. Zhang, D. A. Muller, D. C. Ralph, and R. A. Buhrman, *Advanced Functional Materials* **30**, 2005201 (2020).
- [22] J. W. Lee, J. Y. Park, J. M. Yuk, and B. G. Park, *Physical Review Applied* **13**, 044030 (2020).
- [23] R. Q. Zhang, L. Y. Liao, X. Z. Chen, T. Xu, L. Cai, M. H. Guo, H. Bai, L. Sun, F. H. Xue, J. Su, X. Wang, C. H. Wan, H. Bai, Y. X. Song, R. Y. Chen, N. Chen, W. J. Jiang, X. F. Kou, J. W. Cai, H. Q. Wu, F. Pan, and C. Song, *Physical Review B* **101**, 214418 (2020).
- [24] D. Céspedes-Berrocá, H. Damas, S. Petit-Watelot,

- D. Maccariello, P. Tang, A. Arriola-Córdova, P. Vallobra, Y. Xu, J. Bello, E. Martin, S. Migot, J. Ghanbaja, S. Zhang, M. Hehn, S. Mangin, C. Panagopoulos, V. Cros, A. Fert, and J. Rojas-Sánchez, *Advanced Materials* **33**, 2007047 (2021).
- [25] L. Zhu, D. C. Ralph, and R. A. Buhrman, *Advanced Functional Materials* **31**, 2103898 (2021).
- [26] Q. Liu, L. Zhu, X. S. Zhang, D. A. Muller, and D. C. Ralph, *Applied Physics Reviews* **9**, 021402 (2022).
- [27] Z. Chen, M. Yi, M. Chen, S. Li, S. Zhou, and T. Lai, *Applied Physics Letters* **101**, 222402 (2012).
- [28] X. Ma, L. Ma, P. He, H. B. Zhao, S. M. Zhou, and G. Lüpke, *Physical Review B* **91**, 014438 (2015).
- [29] M. A. W. Schoen, J. Lucassen, H. T. Nembach, T. J. Silva, B. Koopmans, C. H. Back, and J. M. Shaw, *Physical Review B* **95**, 134411 (2017).
- [30] M. Oogane, T. Wakitani, S. Yakata, R. Yilgin, Y. Ando, A. Sakuma, and T. Miyazaki, *Japanese Journal of Applied Physics* **45**, 3889 (2006).
- [31] C. Du, H. Wang, F. Yang, and P. C. Hammel, *Physical Review B* **90**, 140407 (2014).
- [32] M. W. Keller, K. S. Gerace, M. Arora, E. K. Delczeg-Czirjak, J. M. Shaw, and T. J. Silva, *Physical Review B* **99**, 214411 (2019).
- [33] E. R. Edwards, H. T. Nembach, and J. M. Shaw, *Physical Review Applied* **11**, 054036 (2019).
- [34] K. Gilmore, Y. U. Idzerda, and M. D. Stiles, *Physical Review Letters* **99**, 027204 (2007).
- [35] B. Khodadadi, A. Rai, A. Sapkota, A. Srivastava, B. Nepal, Y. Lim, D. A. Smith, C. Mewes, S. Budhathoki, A. J. Hauser, M. Gao, J.-F. Li, D. D. Viehland, Z. Jiang, J. J. Heremans, P. V. Balachandran, T. Mewes, and S. Emori, *Physical Review Letters* **124**, 157201 (2020).
- [36] B. Heinrich, Spin relaxation in magnetic metallic layers and multilayers, *Ultrathin Magnetic Structures III* 143-210, Springer (2005).
- [37] J. M. Shaw, H. T. Nembach, and T. J. Silva, *Applied Physics Letters* **99** (2011).
- [38] P. Omelchenko, E. A. Montoya, C. Coutts, B. Heinrich, and E. Girt, *Scientific Reports* **7**, 1 (2017).
- [39] C. K. A. Mewes and T. Mewes, Relaxation in magnetic materials for spintronics, *Handbook of Nanomagnetism*, 75-91, Stanford (2015).
- [40] K. Zakeri, J. Lindner, I. Barsukov, R. Meckenstock, M. Farle, U. von Hörsten, H. Wende, W. Keune, J. Rucker, S. S. Kalarickal, K. Lenz, W. Kuch, K. Baberschke, and Z. Fraai, *Physical Review B* **76**, 104416 (2007).
- [41] S. Wu, D. A. Smith, P. Nakarmi, A. Rai, M. Clavel, M. K. Hudait, J. Zhao, F. M. Michel, C. Mewes, T. Mewes, and S. Emori, *Physical Review B* **105**, 174408 (2022).
- [42] K. Gilmore, M. D. Stiles, J. Seib, D. Steiauf, and M. Fähnle, *Physical Review B* **81**, 174414 (2010).
- [43] D. A. Smith, A. Rai, Y. Lim, T. Q. Hartnett, A. Sapkota, A. Srivastava, C. Mewes, Z. Jiang, M. Clavel, M. K. Hudait, D. D. Viehland, J. J. Heremans, P. V. Balachandran, T. Mewes, and S. Emori, *Physical Review Applied* **14**, 034042 (2020).
- [44] G. S. Abo, Y.-K. Hong, J. Park, J. Lee, W. Lee, and B.-C. Choi, *IEEE Transactions on Magnetics* **49**, 4937 (2013).
- [45] K. Niitsu, *Journal of Physics D: Applied Physics* **53**, 39LT01 (2020).
- [46] Y. Lim, B. Khodadadi, J.-F. Li, D. Viehland, A. Manchon, and S. Emori, *Physical Review B* **103**, 024443 (2021).
- [47] S. S. Kalarickal, P. Krivosik, M. Wu, C. E. Patton, M. L. Schneider, P. Kabos, T. J. Silva, and J. P. Nibarger, *Journal of Applied Physics* **99**, 093909 (2006).
- [48] L. Liu, T. Moriyama, D. C. Ralph, and R. A. Buhrman, *Physical Review Letters* **106**, 036601 (2011).
- [49] S. Karimeddiny and D. C. Ralph, *Physical Review Applied* **15**, 064017 (2021).
- [50] M. H. Nguyen and C. F. Pai, *APL Materials* **9** 030902 (2021).
- [51] K. Kondou, H. Sukegawa, S. Kasai, S. Mitani, Y. Niimi, and Y. Otani, *Applied Physics Express* **9**, 023002 (2016).
- [52] A. Okada, Y. Takeuchi, K. Furuya, C. Zhang, H. Sato, S. Fukami, and H. Ohno, *Physical Review Applied* **12**, 014040 (2019).
- [53] H. Schultheiss, J. E. Pearson, S. D. Bader, and A. Hoffmann, *Physical Review Letters* **109**, 237204 (2012).
- [54] D. Jiang, H. Chen, G. Ji, Y. Chai, C. Zhang, Y. Liang, J. Liu, W. Skowroński, P. Yu, D. Yi, and T. Nan, *Physical Review Applied* **21**, 024021 (2024).
- [55] S. Kasai, K. Kondou, H. Sukegawa, S. Mitani, K. Tsukagoshi, and Y. Otani, *Applied Physics Letters* **104**, 092408 (2014).
- [56] T. Nan, S. Emori, C. T. Boone, X. Wang, T. M. Oxholm, J. G. Jones, B. M. Howe, G. J. Brown, and N. X. Sun, *Physical Review B* **91**, 214416 (2015).
- [57] W. Wang, T. Wang, V. P. Amin, Y. Wang, A. Radhakrishnan, A. Davidson, S. R. Allen, T. J. Silva, H. Ohldag, D. Balzar, B. L. Zink, P. M. Haney, J. Q. Xiao, D. G. Cahill, V. O. Lorenz, and X. Fan, *Nature Nanotechnology* **14**, 819–824 (2019).
- [58] N. Soya, M. Yamada, K. Hamaya, and K. Ando, *Phys. Rev. Lett.* **131**, 076702(2023).
- [59] C. Kim, D. Kim, B. S. Chun, K.-W. Moon, and C. Hwang, *Physical Review Applied* **9**, 054035 (2018).
- [60] R. W. Greening, D. A. Smith, Y. Lim, Z. Jiang, J. Barber, S. Dail, J. J. Heremans, and S. Emori, *Applied Physics Letters* **116**, 052402 (2020).
- [61] O. Inyang, C. Swindells, D. Rianto, L. Bouchenoire, R. J. Morris, A. Merkulov, A. Caruana, C. Kinane, T. P. Hase, and D. Atkinson, *Applied Physics Letters* **123**, 122403 (2023).
- [62] Reflectometry software, Ref1d, NIST, available at <https://www.nist.gov/ncnr/data-reduction-analysis/reflectometry-software>.
- [63] M. R. Fitzsimmons and C. F. Majkrzak, *Modern Techniques for Characterizing Magnetic Materials*, 107, Springer (2005).
- [64] M. A. W. Schoen, J. Lucassen, H. T. Nembach, T. J. Silva, B. Koopmans, C. H. Back, and J. M. Shaw, *Physical Review B* **95**, 134410 (2017).
- [65] S. Bandiera, R. R. Sousa, B. B. Rodmacq, and B. Dieny, *IEEE Magnetics Letters* **2** (2011).
- [66] P. P. J. Haazen, E. Murè, J. H. Franken, R. Lavrijsen, H. J. M. Swagten, and B. Koopmans, *Nature Materials* **12**, 299 (2013).
- [67] S.-G. Je, D.-H. Kim, S.-C. Yoo, B.-C. Min, K.-J. Lee, and S.-B. Choe, *Physical Review B* **88**, 214401 (2013).
- [68] T. Noma, K. Takada, and A. Iida, *X-ray Spectrometry* **28**, 433 (1999).
- [69] P. Colombi, P. Zanola, E. Bontempi, R. Roberti, M. Gelfi, and L. E. Depero, *Journal of Applied Crystallography*

- 39**, 176 (2006).
- [70] M. Filianina, J. P. Hanke, K. Lee, D. S. Han, S. Jaiswal, A. Rajan, G. Jakob, Y. Mokrousov, and M. Kläui, *Physical Review Letters* **124**, 217701 (2020).
- [71] G. D. H. Wong, Z. Xu, W. Gan, C. C. I. Ang, W. C. Law, J. Tang, W. Zhang, P. K. J. Wong, X. Yu, F. Xu, A. T. Wee, C. S. Seet, and W. S. Lew, *ACS Nano* **15**, 8319 (2021).
- [72] D. Go, D. Jo, C. Kim, and H.-W. Lee, *Physical Review Letters* **121**, 086602 (2018).
- [73] D. Go and H. W. Lee, *Physical Review Research* **2**, 013177 (2020).
- [74] T. Seki, Y.-C. Lau, S. Iihama, and K. Takahashi, *Physical Review B* **104**, 094430 (2021).
- [75] Q. Fu, L. Liang, W. Wang, L. Yang, K. Zhou, Z. Li, C. Yan, L. Li, H. Li, and R. Liu, *Physical Review B* **105**, 224417 (2022).
- [76] X-ray refractive index calculator, TU Wien, available at <https://gixa.ati.tuwien.ac.at/tools/refractive.xhtml>.